Chemical Physics Letters 683 (2017) 91–95

Contents lists available at ScienceDirect

Chemical Physics Letters

journal homepage: www.elsevier.com/locate/cplett

Research paper

OD + CO → D + CO_2 branching kinetics probed with time-resolved frequency comb spectroscopy

Thinh Q. Bui *, Bryce J. Bjork, P. Bryan Changala, Oliver H. Heckl, Ben Spaun, Jun Ye *

JILA, National Institute of Standards and Technology and University of Colorado, Department of Physics, University of Colorado, Boulder, CO 80309, USA

ARTICLE INFO

Article history:
Received 30 December 2016
In final form 18 April 2017
Available online 19 April 2017

ABSTRACT

Time-resolved direct frequency comb spectroscopy was used to study the kinetics of the OD + CO → D + CO_2 reaction, which is important for atmospheric and combustion chemistry. Complementing our recent work on quantifying the formation rate of the *trans*-DOCO radical, we report measurements of the kinetics of the chemically activated product channel, D + CO_2, at room temperature. Simultaneous measurements of the time-dependence of OD and CO_2 concentrations directly yield the products' formation rate and its dependence on pressure and bath gas. Together with the *trans*-DOCO formation rate, these new measurements provide absolute yields of branching channels for both products of OD + CO in the low-pressure limit.

Published by Elsevier B.V.

1. Introduction

The reaction,

$$OH + CO \xrightarrow{k_1} H + CO_2, \quad (1)$$

has served as a benchmark system for kinetics and dynamics studies of complex-forming, bimolecular reactions for the past four decades because of its importance in atmospheric and combustion chemistry [1]. On Earth, CO is a byproduct of fossil fuel burning and hydrocarbon oxidation and acts as a global sink for OH radicals in the free troposphere. In fossil fuel combustion, reaction (1) is the main oxidation step to convert CO to CO_2. Based on a recent proposal by Boxe et al. [2], the OH + CO reaction may also play a significant role in explaining the CO_2 budget on Mars: reactions involving the long-lived HOCO radical intermediate may be a key catalytic source of CO_2 production.

The OH + CO reaction is given by the following elementary reaction steps:

$$OH + CO \underset{k_r}{\overset{k_f}{\rightleftharpoons}} HOCO^* \quad (2)$$

$$HOCO^* \xrightarrow[[M]]{k_2} HOCO \quad (3)$$

$$HOCO^* \xrightarrow{k_3} H + CO_2 \quad (4)$$

The OH + CO proceeds to first form the (vibrationally) energized $HOCO^*$, which can (i) dissociate back to OH + CO, (ii) relax to ground state HOCO by third-body collisions with bath gas M, at a rate coefficient k_{1a}, and/or (iii) decompose to produce the activated products, H + CO_2, at a rate coefficient k_{1b}. The formation of the HOCO radical complex leads to the observed non-Arrhenius temperature and strong pressure dependence of the rate coefficient [3–7]. Based on this scheme, HOCO and H + CO_2 formation dominate in the high- and low-pressure limits, respectively. The overall reaction rate, k_1, is simply described by an effective bimolecular rate constant $k_1([M],T) = k_{1a}([M],T) + k_{1b}([M],T)$.

The temperature and pressure dependence of the OH + CO rate coefficients has been studied extensively [3–15]. Purely *ab initio* methods involving master equations can provide estimates for thermal rate coefficients of complex-forming, pressure-dependent reactions; however, such endeavors are often hindered by incomplete accounting of collision and energy transfer dynamics for activation and stabilization of intermediate complexes [16,17]. Moreover, the rate coefficients are particularly sensitive to the collisional and energy transfer parameters in the low-pressure limit and fall-off regions (intermediate pressure range between the low- and high-pressure limits). In the case of the OH + CO reaction, these problems have persisted for over four decades. The underlying dynamics involving the HOCO radical intermediate have previously been understood only in terms of empirical fit models [4,6,9,10,18] and master equation calculations [1,19,20] used to fit the measured decay rate coefficients of OH in the presence of CO, k_1 [17]. Experimentally, quantitative kinetic measurements of pressure-dependent branching, i.e. stabilization to HOCO (Eq. (3)) and activation to H + CO_2 (Eq. (4)), are necessary

* Corresponding authors.
E-mail addresses: thbu8553@jila.colorado.edu (T.Q. Bui), ye@jila.colorado.edu (J. Ye).

http://dx.doi.org/10.1016/j.cplett.2017.04.061
0009-2614/Published by Elsevier B.V.

prerequisites. Yet, the HOCO intermediate has eluded detection in thermal environments until recent experimental demonstration by Bjork et al. [21] on the first direct measurements of the formation rate (k_{1a}) of the deuterated analogue, *trans*-DOCO, in the OD + CO reaction. This study complements the Bjork et al. work in providing the direct measurements of the formation rate (k_{1b}) of the activated products, D + CO_2, at thermal conditions using frequency comb spectroscopy. Together, the goal of these studies is to provide quantitative, mechanistic details of the OD + CO reaction in the low-pressure limit, a good test case for studying effects of collisional energy transfer on rate coefficients for this important complex-forming reaction.

2. Experimental

Time-resolved frequency comb spectroscopy (TRFCS) has been developed for applications to spectroscopy and dynamics of transient radicals [22,23]. Relevant details for this experiment are found in our previous publication [21]. A high repetition rate (f_{rep} = 136 MHz) mode-locked femtosecond fiber laser synchronously pumps an optical parametric oscillator (OPO) to produce the mid-IR comb light spanning from 3 to 5 μm [24]. The mid-IR comb light is injected into a high-finesse cavity, the free spectral range (FSR) of which is matched and locked to $2 \times f_{rep}$. The transmitted light is spatially dispersed by a virtually-imaged phased array (VIPA) etalon and a grating combination, which is then imaged onto an InSb camera and recorded with an integration time ≥10 μs [25]. Absorption spectra as a function of time are constructed from the camera images and fitted to known line intensities of reference molecular spectra to obtain absolute concentrations. In general, this technique provides a unique combination of broad bandwidth spectroscopy, high sensitivity, high spectral resolution and microseconds time resolution for simultaneous detection of a number of key species in the reaction. The main modification to the previous TRFCS instrument is the use of high finesse mirrors centered at 3.92 μm. Mid-IR mirror finesse measurements were conducted in the same manner described by Cole et al. [26] These mirrors provide both a high finesse (F ≈ 5600) and a large bandwidth (>400 nm), as shown in Fig. 1. The large bandwidth provides access to many molecular species relevant to the OD + CO reaction including *trans*-DOCO, CO_2, DO_2, D_2O, and OD(v = 0–4). All of these have been measured in this experiment except for OD(v = 3, 4).

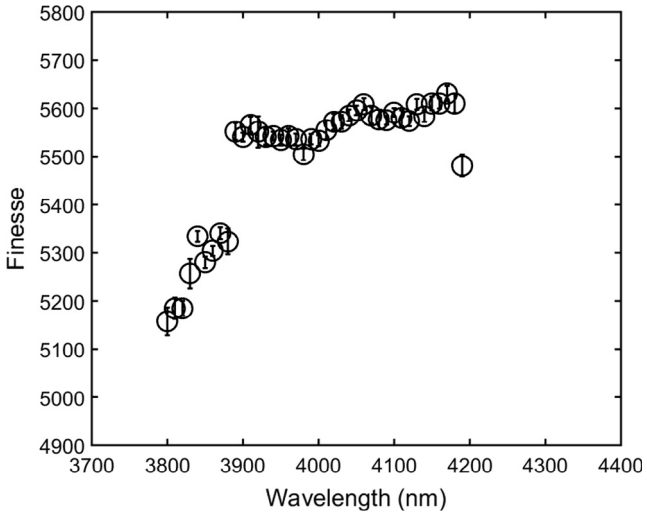

Fig. 1. Measured finesse curve for high reflectivity mirrors centered at 3.92 μm. The large bandwidth (>400 nm) provides access to most molecular species relevant to the OD + CO reaction, including *trans*-DOCO, CO_2, DO_2, D_2O, and OD(v = 0–4).

The OD + CO reaction was studied in a flow cell under reaction conditions kept nearly the same as those described by Bjork et al. Major sources of systematic error have been characterized under these conditions, including rate constant dependence on camera integration time, vibrationally excited OD contributions, and O_3 and D_2 gas concentrations. Here, we will provide only a brief summary of the experimental procedures. $O(^1D)$ atoms are first generated from photolysis of O_3 at 266 nm (35 mJ/pulse) from a frequency-quadrupled Nd:YAG laser. Each photolysis pulse dissociates about 15% of the ozone to form $O(^1D)$ and O_2. In the presence of D_2, $O(^1D) + D_2$ produces energized OD(v = 0–4) with an inverted population peaking at v = 2 and v = 3 [27]. D_2O_2 could serve as an alternative source for OD, but its strong absorption in the OD and *trans*-DOCO spectral regions would reduce sensitivity and increase spectral congestion. High CO concentrations (>3.5×10^{17} - molecules cm^{-3}) were maintained for the purpose of ensuring the low densities and short lifetimes of OD(v > 0). The OD(v = 1) + CO quenching rate constant was previously measured to be 3.3 (2) $\times 10^{-13}$ cm^3 $molecules^{-1}$ s^{-1} [21]. Using this value, the maximum lifetime (1/e) of OD(v = 1) at our conditions is 8.7 μs. Maintaining a concentration of high CO ensures that the contribution from vibrationally excited OD on the uncertainties of k_{1b} is less than 10% based on both the lifetime and abundance detection sensitivity of OD(v > 0).

Molecular densities of D_2, CO and N_2 were controlled and monitored with mass flow regulators and meters. For all experiments, the O_3 concentration was fixed at 2×10^{15} molecules cm^{-3} and monitored *in situ* by UV absorption spectroscopy at 270 nm. The D_2 concentration was also kept constant at 7.4×10^{16} molecules cm^{-3}. By controlling the partial pressures of He, CO, and N_2 gases, the experimental total pressures were varied from 40 to 120 torr.

3. Results and discussion

Absorption spectra covering ≈60 cm^{-1} of bandwidth (limited by the size of the camera detector area) centered at 2420 cm^{-1} (≈4.13 μm) were recorded with a varying time delay from the t = 0 photolysis pulse. Each spectrum was normalized to a reference spectrum acquired immediately before the photolysis pulse and fitted to determine the time-dependent concentrations. For all experiments, the camera integration time was fixed at 100 μs. Fig. 2a show representative snapshots of measured and simulated spectra at time delays of 25 and 1000 μs after the photolysis pulse. The R(76) transition of CO_2 near 2390.522 cm^{-1} (line intensity S = 4.140×10^{-22} cm $molecule^{-1}$) and OD transition near 2433.6 cm^{-1} (S = 1.64×10^{-21} cm $molecule^{-1}$) are the strongest absorption features. The time-dependent curves in Fig. 2b were obtained from fitting integrated areas for both molecules. The OD line intensities are determined from transition dipole moments calculated using the empirical potential energy and dipole moment surfaces reported by Nesbitt and coworkers [28,29]. The CO_2 line intensities were taken from the HITRAN 2012 database [30].

The rate coefficients for the D + CO_2 channel, $k_{1b}([M],T)$, were determined from simultaneous measurements of time-dependent $[CO_2](t)$ and $[OD](t)$. k_{1b} may be bimolecular (independent of pressure) or termolecular, depending on whether the conditions are at the low, intermediate, or high-pressure limits [4,6,18]. We evaluated these scenarios by measuring the dependence of the effective bimolecular rate constant on the concentrations of CO, N_2, and He.

The time-dependent CO_2 formation rate is given by the rate equation

$$\frac{d[CO_2]}{dt} = k_{1b}[CO][OD](t), \quad (5)$$

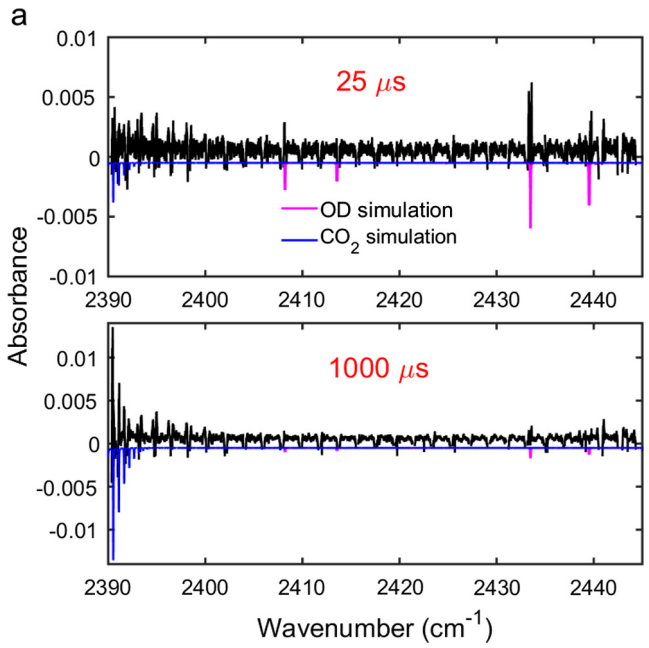

Fig. 2a. Measured spectra (black) at 25 and 1000 μs delay from the photolysis pulse. These spectra are fitted to reference OD(v = 0) (magenta) and CO_2 (blue) spectra to acquire the temporal profile. The decay of OD(v = 0) and the rise of CO_2 are apparent between 25 and 1000 μs delay. (For interpretation of the references to colour in this figure legend, the reader is referred to the web version of this article.)

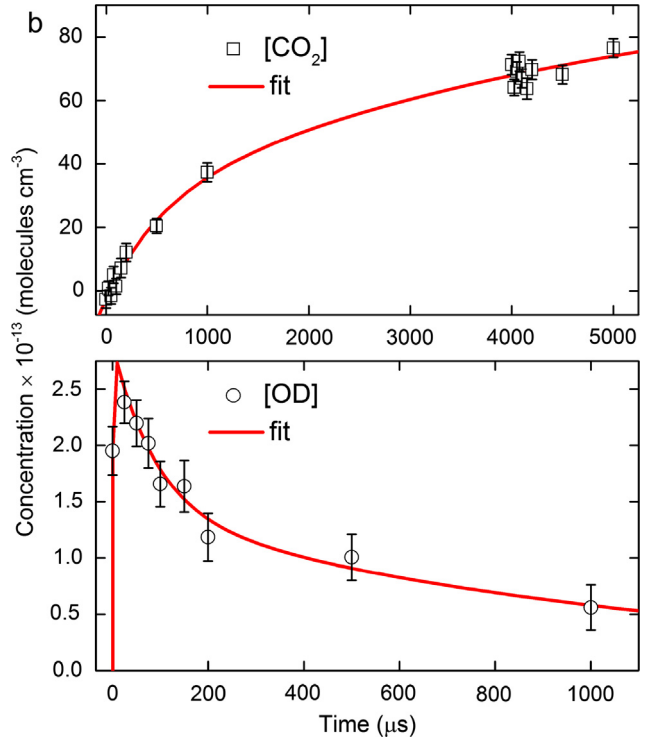

Fig. 2b. (Bottom) An analytical functional form for [OD](t) is obtained from fitting the data (black circles) to a sum of box-car averaged exponential rise and fall functions (red line). (Top) The rise rate of CO_2 is obtained from fitting the data (black squares) to Eq. (6) (red line). The error bars correspond to 1σ uncertainties, which include contributions from uncertainties from the spectral fits and concentration measurements. The camera integration time was fixed at 100 μs. (For interpretation of the references to colour in this figure legend, the reader is referred to the web version of this article.)

where [OD](t) refers to time-dependent concentration of OD in the vibrational ground state. Contrary to DOCO, which reacts with O_3, CO_2 does not have a large loss channel on the time scale (<1 ms) of our rate constant determination. Solving Eq. (5) for [CO_2](t) gives

$$[CO_2](t) = k_{1b}[CO]\int_0^t [OD](u)du. \quad (6)$$

Since [CO] is in large excess and remains constant throughout the reaction, quantifying k_{1b} requires only the time dependence of [CO_2] and [OD]. For [OD](t), we fit the data using derived analytical functions comprised of the sum of exponential rise and fall functions. These exponential functions are convolved with a 100 μs time-window to simulate the behavior of the boxcar-averaging originating from the temporal response of the camera. Eq. (6) gives the functional form for fitting [CO_2](t), where [OD](t) is from the fitted time window of 0 to 1000 μs. Finally, k_{1b} may depend on bath gas and pressure, i.e.,

$$k_{1b} = k_{1b}^{(CO)}[CO] + k_{1b}^{(N2)}[N_2] + k_{1b}^{(He)}[He]. \quad (7)$$

Representative plots of fits to both [CO_2](t) and [OD](t) are shown in Fig. 2b. The boxcar-convolved fits for [CO_2](t) and [OD](t) reveal the presence of multiple competing time-dependent processes, which are expected due to the secondary regeneration channels of OD. At our conditions, OD decay is observed to be bi-exponential, with the initial decay (lifetime ≈ 100–300 μs) coming from reactions with CO. The second exponential decay (lifetime ≈ 1000 μs) occurs approximately after 300 μs and [OD] reaches a near steady-state at longer times (t > 1000 μs). OD regeneration reactions $D + O_3 \rightarrow OD + O_2$ and $DOCO + O_3 \rightarrow OD + CO_2 + O_2$ dominate at longer times, consistent with previous observations [4,21]. Therefore, only the earliest time behavior (<300 μs) captures the initial $OD + CO \rightarrow D + CO_2$ branching reaction and is used for the analysis of k_{1b}.

The bath gas and pressure dependence of the bimolecular rate constant k_{1b} were measured for CO, N_2 and He gas. For CO, the range of densities was limited from 3.5×10^{17} to 1.0×10^{18} molecules cm^{-3}. Low CO densities were avoided due to complications from vibrationally excited OD since CO is an efficient quencher of OD vibration. High CO densities limit the signal-to-noise of OD detection because of $O(^1D) + CO$ quenching. The effects of vibrationally excited OD in this system have been systematically analyzed previously [21]. For N_2 and He gas, the upper limit densities of ≈3.5×10^{18} molecules cm^{-3} were dictated by technical limitations: high molecular densities result in large mechanical vibrations which affect cavity locking stability. The results of the k_{1b} measurements are shown in Fig. 3. Within 1σ statistical uncertainties, k_{1b} was observed to be constant with respect to pressure for all three bath gases. The averaged k_{1b} values are $5.6(7) \times 10^{-14}$, $6.6(8) \times 10^{-14}$, and $6.1(7) \times 10^{-14}$ cm^3 $molecules^{-1}$ s^{-1} for CO, N_2, and He, respectively. We experimentally investigated another possible source of systematic error for k_{1b} arising from the reaction $DOCO + O_3 \rightarrow CO_2 + OD + O_2$, which would contribute an additional source of CO_2. To provide a quantitative estimate from this channel, we measured k_{1b} as a function of O_3 density ($2–4.5 \times 10^{15}$ molecules cm^{-3}), and observed no dependence (fit of a flat line to the data yielded a reduced $\chi^2 \approx 0.3$) within the statistical uncertainty. This observation is consistent with the fact that the concentration of DOCO is much smaller by more than an order of magnitude compared to that of CO_2. Therefore, DOCO + O_3 can contribute at most 10% error to our measured k_{1b}, which has been accounted for in our uncertainty budget.

The observed k_{1b} results may be rationalized from unimolecular rate theory and the associated Lindemann mechanism common to pressure-dependent reaction kinetics [4,6,18]. Starting from pro-

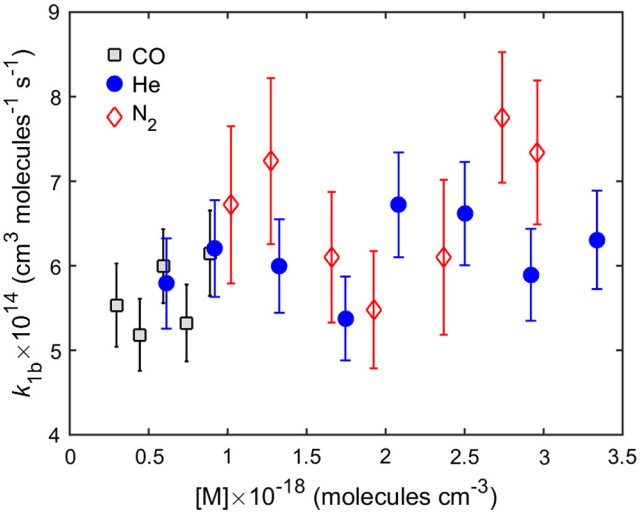

Fig. 3. The formation rate (k_{1b}) of the activated products, D + CO_2, as a function of bath gases (M = N_2 (red diamond), CO (black squares), He (blue circles)) and pressure. k_{1b} is calculated according to Eq. (6). The error bars correspond to 1σ uncertainties, which include contributions from uncertainties from the fits to Eq. (6) and concentration measurements. (For interpretation of the references to colour in this figure legend, the reader is referred to the web version of this article.)

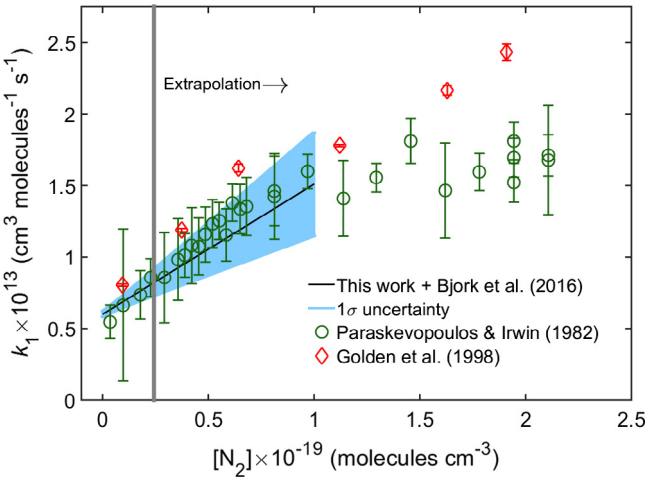

Fig. 4. Comparison of the bimolecular rates, $k_1([M],T) = k_{1a}([M],T) + k_{1b}([M],T)$, for OD + CO in N_2 bath gas at room temperature. The solid black line is the calculated sum of k_{1a} from Bjork et al. and k_{1b} from this work with its 1σ uncertainty in shaded teal. k_1 for OD + CO in N_2 has been reported by Paraskevopoulos & Irvin (green circles) and Golden et al. (red diamonds). The gray vertical line marks the divide between the experimental (left) and extrapolated (right) pressure regions. (For interpretation of the references to colour in this figure legend, the reader is referred to the web version of this article.)

cesses described in Eqs. (2)–(4) and applying the steady-state approximation (d[DOCO*]/dt = 0), the CO_2 formation rate is

$$\frac{d[CO_2]}{dt} = \frac{k_f k_2}{k_r + k_2 + k_3[M]}[OD][CO]. \quad (8)$$

Recasting the first factor in Eq. (8) and applying the limits of [M] → 0 and [M] → ∞ yield the low- and high-pressure limit rate constants given by Eqs. (9) and (10), respectively:

$$k_{1b,[M]\to 0} \approx \frac{k_f k_2}{k_r + k_2}, \quad (9)$$

$$k_{1b,[M]\to \infty} \approx \frac{k_f k_2}{k_3[M]}. \quad (10)$$

Here, k_{1b} is independent of [M] as pressure approaches zero and inversely proportional to [M] at infinite pressure. The experimentally observed pressure-independent behavior of k_{1b} is consistent with predictions by this Lindemann-type mechanism in the low-pressure limit Eqs. (8) and (9). Similar observations were reported previously from empirical fits to k_1 from literature measurements in the low-pressure limit, as discussed in detail by Fulle et al. [4] and Golden et al. [6] Any apparent curvature in the pressure dependence would suggest deviations from the Lindemann mechanism or departure from the low-pressure limit and transition into the fall-off region, which we cannot completely rule out given our measurement uncertainties of k_{1b} shown in Fig. 3.

Based on k_{1a} from Bjork et al. and k_{1b} from this work, we can directly compare our measured values to literature measurements of k_1. According to calculations by Weston et al. [19] and the empirically-derived forms of k_{1a} and k_{1b} from Fulle et al., most of the pressure-dependence of k_1 comes from k_{1a} in the low-pressure limit. These previous observations are qualitatively consistent with our own measurements of k_{1a} and k_{1b}. Since k_{1b} is constant within the pressure range studied, it represents a constant offset to the amplitude of k_1. Two measurements of the rate constant k_1 for OD + CO in N_2 bath gas have been reported by Paraskevopoulos et al. [9] and Golden et al. [6] at room temperature. The comparisons are shown in Fig. 4. By calculating the quantity $k_1 = k_{1a}^{(N2)}[N_2] + k_{1b}$, the black solid line is obtained. Here, $k_{1a}^{(N2)}$ is the termolecular rate coefficient for *trans*-DOCO formation in N_2 bath gas measured by Bjork et al. The shaded teal region is the 1σ error for the calculated k_1. Because k_{1a} was only measured up to 75 torr, the vertical gray line is the demarcation of measured versus extrapolated regions of k_1. The good agreement with Paraskevopoulos et al. and Golden et al. provides quantitative validation for treating OD + CO in the low-pressure limit as a simple sum of the collision-induced association (k_{1a}) and chemically activated reaction (k_{1b}). As discussed by Fulle et al., one would expect that this treatment breaks down at much higher pressures upon the transition into the fall-off region, where more sophisticated modeling, e.g. Troe [31] corrections, RRKM [32] theory, etc., would be required. Master-equation calculations by Weston et al. predict curvature in k_1 (Fig. 9 in their text) for OD + CO in He gas for our experimental pressure range, which we do not observe within our measurement uncertainties. We also note that our measured value of k_1 in He at the zero pressure limit is $6.1(7) \times 10^{-14}$ cm^3 $molecules^{-1}$ s^{-1}, slightly higher than the reported values of 3.87×10^{-14} cm^3 $molecules^{-1}$ s^{-1} by Weston et al. Finally, the *cis*-DOCO isomer may also have a non-negligible k_{1a} contribution that has been unquantified to date.

Using the k_{1a} reported by Bjork et al., we can also determine the branching yield for DOCO and D + CO_2 channels in N_2 and CO gas for the OD + CO reaction. Previous DOCO yield calculations [21] were made under the assumption that $k_{1b} = k_1$ at zero pressure by using an averaged k_1 value from Paraskevopoulos et al., Golden et al., and Westerberg et al. [33] We can now check the validity of this assumption by using the measured k_{1b} in this work. The branching yield of DOCO is given by $k_{1a}/(k_{1a} + k_{1b})$. At the highest pressure of 75 torr, the DOCO yield in N_2 gas is 27 ± 11%. and the corresponding D + CO_2 yield is 73 ± 16%. This measured DOCO yield in N_2 is equivalent within 1σ to those calculated by Bjork et al., and it is now supported with direct experimental validation. For CO bath gas, the same measurement procedure gives yields of 47 ± 10% and 53 ± 7% for DOCO and D + CO_2, respectively.

4. Conclusion

In this work, the OD + CO product branching to D + CO_2 has been quantified within the low-pressure limit. In conjunction with

our previous k_{1a} work, these results provide experimental evidence for the mass balance of OD + CO product branching, whose sum yields the observed literature measurement of k_1. This work demonstrates another realization of the potential of optical frequency combs for studying complex chemistry problems: For systems like OD + CO that involve multiple intermediates and products, the inherent flexibility of time-resolved direct frequency comb spectroscopy allows for a comprehensive, quantitative, and deterministic exploration of detailed reaction mechanisms. The applications of frequency combs for studying many other classes of chemical reactions will only continue to grow with improved comb sources at higher powers and longer wavelength beyond the mid-IR [34,35], as well as progress in high finesse mirror technology. Another powerful future direction for this technique is to access a wide range of temperatures provided by buffer gas cooling [36,37], accessing a thermalized and cold (<10 K) reaction environment.

Acknowledgements

We acknowledge financial support from AFOSR, DARPA SCOUT, ARO-MURI, NIST, and the Physics Frontier Center at JILA (NSF). T.Q. Bui and B. Spaun are supported by the National Research Council Research Associate Fellowship, P.B. Changala is supported by the NSF GRFP, and O.H. Heckl is partially supported through a Humboldt Fellowship. Finally, we thank Mitchio Okumura at Caltech for helpful discussions and insights on the OD + CO work.

References

[1] T.L. Nguyen, B.C. Xue, R.E. Weston, J.R. Barker, J.F. Stanton, J. Phys. Chem. Lett. 3 (11) (2012) 1549–1553.
[2] C.S. Boxe, J.S. Francisco, R.L. Shia, Y.L. Yung, H. Nair, M.C. Liang, A. Saiz-Lopez, Icarus 242 (2014) 97–104.
[3] A.R. Ravishankara, R.L. Thompson, Chem. Phys. Lett. 99 (5–6) (1983) 377–381.
[4] D. Fulle, H.F. Hamann, H. Hippler, J. Troe, J. Chem. Phys. 105 (3) (1996) 983–1000.
[5] I.W.M. Smith, R. Zellner, J. Chem. Soc.-Faraday Trans. 69 (11) (1973) 1617.
[6] D.M. Golden, G.P. Smith, A.B. McEwen, C.L. Yu, B. Eiteneer, M. Frenklach, G.L. Vaghjiani, A.R. Ravishankara, F.P. Tully, J. Phys. Chem. A 102 (44) (1998) 8598–8606.
[7] M.J. Frost, P. Sharkey, I.W.M. Smith, J. Phys. Chem. 97 (47) (1993) 12254–12259.
[8] D.C. McCabe, T. Gierczak, R.K. Talukdar, A.R. Ravishankara, Geophys. Res. Lett. 28 (16) (2001) 3135–3138.
[9] G. Paraskevopoulos, R.S. Irwin, Chem. Phys. Lett. 93 (2) (1982) 138–143.
[10] G. Paraskevopoulos, R.S. Irwin, J. Chem. Phys. 80 (1) (1984) 259–266.
[11] M.J. Frost, P. Sharkey, I.W.M. Smith, Faraday Discuss. 91 (1991) 305–317.
[12] J. Brunning, D.W. Derbyshire, I.W.M. Smith, M.D. Williams, J. Chem. Soc.-Faraday Trans. 2 (84) (1988) 105–119.
[13] R. Zellner, J. Phys. Chem. 83 (1) (1979) 18–23.
[14] R. Forster, M. Frost, D. Fulle, H.F. Hamann, H. Hippler, A. Schlepegrell, J. Troe, J. Chem. Phys. 103 (8) (1995) 2949–2958.
[15] Y.D. Liu, S.P. Sander, J. Phys. Chem. A 119 (39) (2015) 10060–10066.
[16] A.W. Jasper, K.M. Pelzer, J.A. Miller, E. Kamarchik, L.B. Harding, S.J. Klippenstein, Science 346 (6214) (2014) 1212–1215.
[17] A.W. Jasper, J.A. Miller, S.J. Klippenstein, J. Phys. Chem. A 117 (47) (2013) 12243–12255.
[18] C.W. Larson, P.H. Stewart, D.M. Golden, Int. J. Chem. Kinet. 20 (1) (1988) 27–40.
[19] R.E. Weston, T.L. Nguyen, J.F. Stanton, J.R. Barker, J. Phys. Chem. A 117 (5) (2013) 821–835.
[20] J.P. Senosiain, C.B. Musgrave, D.M. Golden, Int. J. Chem. Kinet. 35 (9) (2003) 464–474.
[21] B.J. Bjork, T.Q. Bui, O.H. Heckl, P.B. Changala, B. Spaun, P. Heu, D. Follman, C. Deutsch, G.D. Cole, M. Aspelmeyer, M. Okumura, J. Ye, Science 354 (6311) (2016) 444–448.
[22] M.J. Thorpe, K.D. Moll, R.J. Jones, B. Safdi, J. Ye, Science 311 (5767) (2006) 1595–1599.
[23] A.J. Fleisher, B.J. Bjork, T.Q. Bui, K.C. Cossel, M. Okumura, J. Ye, J. Phys. Chem. Lett. 5 (13) (2014) 2241–2246.
[24] F. Adler, K.C. Cossel, M.J. Thorpe, I. Hartl, M.E. Fermann, J. Ye, Opt. Lett. 34 (9) (2009) 1330–1332.
[25] L. Nugent-Glandorf, T. Neely, F. Adler, A.J. Fleisher, K.C. Cossel, B. Bjork, T. Dinneen, J. Ye, S.A. Diddams, Opt. Lett. 37 (15) (2012) 3285–3287.
[26] G.D. Cole, W. Zhang, B.J. Bjork, D. Follman, P. Heu, C. Deutsch, L. Sonderhouse, J. Robinson, C. Franz, A. Alexandrovski, M. Notcutt, O.H. Heckl, J. Ye, M. Aspelmeyer, Optica 3 (6) (2016) 647–656.
[27] J.E. Butler, R.G. Macdonald, D.J. Donaldson, J.J. Sloan, Chem. Phys. Lett. 95 (3) (1983) 183–188.
[28] D.D. Nelson, A. Schiffman, D.J. Nesbitt, J. Chem. Phys. 90 (10) (1989) 5455–5465.
[29] D.D. Nelson, A. Schiffman, D.J. Nesbitt, D.J. Yaron, J. Chem. Phys. 90 (10) (1989) 5443–5454.
[30] L.S. Rothman, I.E. Gordon, Y. Babikov, A. Barbe, D.C. Benner, P.F. Bernath, M. Birk, L. Bizzocchi, V. Boudon, L.R. Brown, A. Campargue, K. Chance, E.A. Cohen, L.H. Coudert, V.M. Devi, B.J. Drouin, A. Fayt, J.M. Flaud, R.R. Gamache, J.J. Harrison, J.M. Hartmann, C. Hill, J.T. Hodges, D. Jacquemart, A. Jolly, J. Lamouroux, R.J. Le Roy, G. Li, D.A. Long, O.M. Lyulin, C.J. Mackie, S.T. Massie, S. Mikhailenko, H.S.P. Muller, O.V. Naumenko, A.V. Nikitin, J. Orphal, V. Perevalov, A. Perrin, E.R. Polovtseva, C. Richard, M.A.H. Smith, E. Starikova, K. Sung, S. Tashkun, J. Tennyson, G.C. Toon, V.G. Tyuterev, G. Wagner, J. Quant. Spectrosc. Radiat. Transfer 130 (2013) 4–50.
[31] J. Troe, J. Chem. Phys. 75 (1) (1981) 226–237.
[32] R.A. Marcus, J. Chem. Phys. 20 (3) (1952) 359–364.
[33] A.A. Westenberg, W.E. Wilson, J. Chem. Phys. 45 (1) (1966) 338.
[34] O.H. Heckl, B.J. Bjork, G. Winkler, P.B. Changala, B. Spaun, G. Porat, T.Q. Bui, K.F. Lee, J. Jiang, M.E. Fermann, P.G. Schunemann, J. Ye, Opt. Lett. 41 (22) (2016) 5405–5408.
[35] K.C. Cossel, E.M. Waxman, I.A. Finneran, G.A. Blake, J. Ye, N.R. Newbury, J. Opt. Soc. Am. B 34 (1) (2017) 104–129.
[36] B. Spaun, P.B. Changala, D. Patterson, B.J. Bjork, O.H. Heckl, J.M. Doyle, J. Ye, Nature 533 (7604) (2016) 517.
[37] P.B. Changala, B. Spaun, D. Patterson, J.M. Doyle, J. Ye, Appl. Phys. B 122 (12) (2016) 292.